Computers and Mathematics with Applications 65 (2013) 102–115

Contents lists available at SciVerse ScienceDirect

Computers and Mathematics with Applications

journal homepage: www.elsevier.com/locate/camwa

A conservative numerical method for the Cahn–Hilliard equation with Dirichlet boundary conditions in complex domains

Yibao Li, Darae Jeong, Jaemin Shin, Junseok Kim *

Department of Mathematics, Korea University, Seoul 136-713, Republic of Korea

ARTICLE INFO

Article history:
Received 11 January 2012
Received in revised form 10 July 2012
Accepted 22 August 2012

Keywords:
Cahn–Hilliard equation
Dirichlet boundary condition
Complex domain
Unconditionally gradient stable scheme
Multigrid method

ABSTRACT

In this paper we present a conservative numerical method for the Cahn–Hilliard equation with Dirichlet boundary conditions in complex domains. The method uses an unconditionally gradient stable nonlinear splitting numerical scheme to remove the high-order time-step stability constraints. The continuous problem has the conservation of mass and we prove the conservative property of the proposed discrete scheme in complex domains. We describe the implementation of the proposed numerical scheme in detail. The resulting system of discrete equations is solved by a nonlinear multigrid method. We demonstrate the accuracy and robustness of the proposed Dirichlet boundary formulation using various numerical experiments. We numerically show the total energy decrease and the unconditionally gradient stability. In particular, the numerical results indicate the potential usefulness of the proposed method for accurately calculating biological membrane dynamics in confined domains.

© 2012 Elsevier Ltd. All rights reserved.

1. Introduction

In this paper, we consider an efficient and robust numerical scheme for the Cahn–Hilliard (CH) equation with Dirichlet boundary conditions in complex domains. This equation was introduced to model spinodal decomposition and coarsening phenomena in binary alloys [1,2] and it arises from the Helmholtz free energy functional

$$\mathcal{E}(\phi) = \int_{\Omega} \left(F(\phi) + \frac{\epsilon^2}{2} |\nabla \phi|^2 \right) d\mathbf{x},$$

where $\Omega \subset \mathbf{R}^2$ and ϵ is a positive constant. The quantity $\phi(\mathbf{x}, t)$ is defined to be the difference between the mole fractions of binary mixtures (e.g., $\phi(\mathbf{x}, t) = m_\alpha - m_\beta$ where m_α and m_β are the mole fractions of phases α and β). $F(\phi) = 0.25(\phi^2 - 1)^2$ is the Helmholtz free energy per unit volume of a homogeneous system of composition ϕ (see Fig. 1) and $\frac{\epsilon^2}{2}|\nabla\phi|^2$ is a gradient energy.

The Cahn–Hilliard equation takes the form

$$\frac{\partial \phi}{\partial t}(\mathbf{x}, t) = M \Delta \mu(\mathbf{x}, t), \quad \mathbf{x} \in \Omega, \ 0 < t \leq T, \tag{1}$$

$$\mu(\mathbf{x}, t) = F'(\phi(\mathbf{x}, t)) - \epsilon^2 \Delta \phi(\mathbf{x}, t), \tag{2}$$

$$\phi(\mathbf{x}, t) = g(\mathbf{x}), \quad \mathbf{x} \in \partial\Omega, \tag{3}$$

* Corresponding author. Tel.: +82 2 3290 3077; fax: +82 2 929 8562.
E-mail address: cfdkim@korea.ac.kr (J. Kim).
URL: http://math.korea.ac.kr/~cfdkim/ (J. Kim).

0898-1221/$ – see front matter © 2012 Elsevier Ltd. All rights reserved.
doi:10.1016/j.camwa.2012.08.018

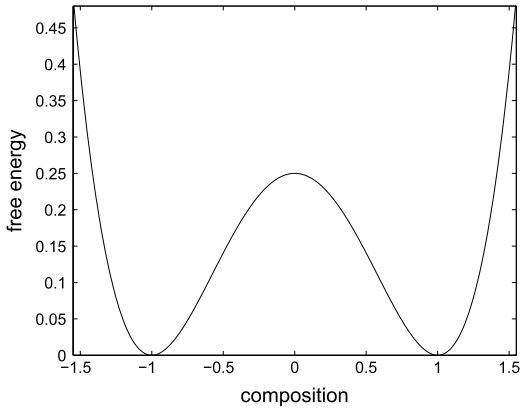

Fig. 1. Helmholtz free energy density $F(\phi) = 0.25(\phi^2 - 1)^2$.

$$\frac{\partial \mu}{\partial n}(\mathbf{x}, t) = 0, \quad \mathbf{x} \in \partial\Omega, \tag{4}$$

where M is a positive constant mobility, $g(\mathbf{x})$ is a given function, and $\mathbf{n}$ is the outward normal vector at the boundary.

To derive Eqs. (1)–(4), we start with mass conservation, i.e.,

$$\phi_t = -\nabla \cdot \mathcal{J}, \tag{5}$$

where the flux is defined as $\mathcal{J} = -M\nabla\mu$. The chemical potential μ can be obtained via the variational derivative of the free energy functional with respect to ϕ, such that

$$\begin{aligned}\frac{d}{d\eta}\mathcal{E}(\phi + \eta v)\Big|_{\eta=0} &= \int_\Omega \left(vF'(\phi) + \epsilon^2 \nabla v \cdot \nabla\phi\right) d\mathbf{x} \\ &= \int_\Omega \left(F'(\phi) - \epsilon^2\Delta\phi\right) v\, d\mathbf{x} + \int_{\partial\Omega} \epsilon^2 \frac{\partial\phi}{\partial n} v\, ds = \int_\Omega \left(F'(\phi) - \epsilon^2\Delta\phi\right) v\, d\mathbf{x},\end{aligned}$$

where v satisfies $\int_\Omega v\, d\mathbf{x} = 0$ and $v = 0$ on $\partial\Omega$. Now we get the chemical potential

$$\mu = \frac{\delta\mathcal{E}}{\delta\phi} = F'(\phi) - \epsilon^2\Delta\phi. \tag{6}$$

Using Eqs. (5) and (6), we get Eq. (1). The CH equation can be derived from a constrained gradient flow in the $\bar{H}^{-1}$ Hilbert space and it guarantees that the total free energy $\mathcal{E}(\phi)$ will decrease in time t [3]. We will show later that the numerical total energy decrease implies the stability of the numerical solutions. The solution $\phi(\mathbf{x}, t)$ of the CH Eqs. (1)–(4) possesses the properties that the total mass $\int_\Omega \phi\, d\mathbf{x}$ is conserved and that the total energy $\mathcal{E}(t)$ decreases with time. That is,

$$\begin{aligned}&\frac{d}{dt}\int_\Omega \phi\, d\mathbf{x} = \int_\Omega \phi_t\, d\mathbf{x} = M\int_\Omega \Delta\mu\, d\mathbf{x} = M\int_{\partial\Omega} \frac{\partial\mu}{\partial n}\, ds = 0, \\ &\frac{d}{dt}\mathcal{E}(t) = \int_\Omega (F'(\phi)\phi_t + \epsilon^2\nabla\phi\cdot\nabla\phi_t) d\mathbf{x} \\ &\quad = \int_\Omega \mu\phi_t d\mathbf{x} + \int_{\partial\Omega} \epsilon^2 \frac{\partial\phi}{\partial n}\phi_t ds = \int_\Omega \mu M\Delta\mu d\mathbf{x} \\ &\quad = \int_{\partial\Omega} \mu M\frac{\partial\mu}{\partial n} ds - \int_\Omega M\nabla\mu\cdot\nabla\mu d\mathbf{x} = -\int_\Omega M|\nabla\mu|^2 d\mathbf{x} \le 0.\end{aligned}$$

Many research papers have been published on the numerical methods for the CH equation [4–35]. Various numerical methods are intensively studied with either Neumann [8–17] or periodic [18–29] boundary condition. Some authors have studied the CH equation with contact angle boundary conditions [30–32]. A few authors have analyzed the Dirichlet problem for the CH equation. Du and Nicolaides [33] proposed a finite element/difference scheme with the property that the total energy decreases with time by using Dirichlet boundary conditions. Bronsard and Hilhorst [34] studied the limiting behavior of the solution of the CH equation with the Dirichlet boundary condition using energy-type methods. In [35], Bates and Han discussed the existence, uniqueness and continuous dependence on initial data of the solution for a nonlocal CH equation with the Dirichlet boundary condition on a bounded domain. While our paper is slightly different from the papers referred to [33–35], we adopt the Neumann boundary condition for μ to keep the mass conservation. Furthermore with Dirichlet boundary conditions, the biharmonic [36], the Schrödinger [37], and the regularized long wave equations [38] were studied.

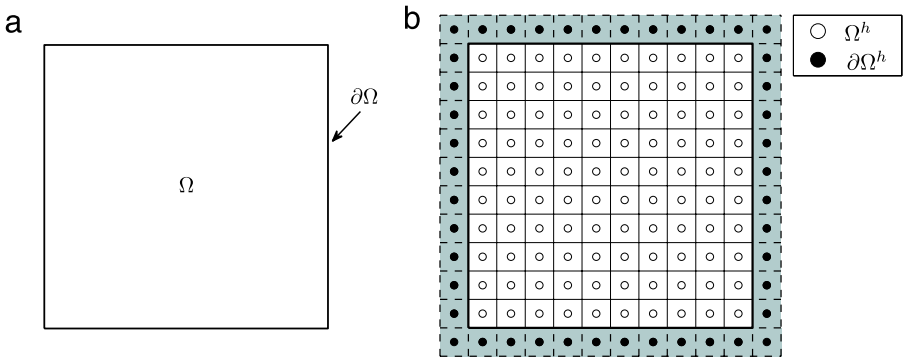

Fig. 2. (a) Domain Ω with boundary $\partial\Omega$ and (b) discrete domain Ω^h with discrete boundary $\partial\Omega^h$.

The possible applications of the CH model with Dirichlet boundary conditions are a non-wetting droplet dynamics in a channel, a red blood cell in capillary blood vessels, and deformation of biological cell morphology in a confined domain [39–52].

The objective of this paper is to propose the conservative numerical method for the Cahn–Hilliard equation with Dirichlet boundary conditions in complex domains. The CH equation is discretized using an unconditionally gradient stability scheme and its resulting scheme is solved by a fast multigrid method.

This paper is organized as follows. In Section 2, we describe the discretization of the CH equation with Dirichlet boundary conditions and its multigrid algorithm. The numerical results, which demonstrate the accuracy and robustness of the proposed Dirichlet boundary formulation, are described in Section 3. A discussion is presented in Section 4.

2. Proposed numerical algorithm with Dirichlet boundary conditions

In this section, we propose a new conservative numerical algorithm for solving the Cahn–Hilliard equation with Dirichlet boundary conditions in complex domains. We discretize the governing Eqs. (1) and (2) in two-dimensional space, i.e., $\Omega = (a, b) \times (c, d)$ and its domain boundary is denoted as $\partial\Omega$ (see Fig. 2(a)). Let $x_i = a + (i - 0.5)h$, $y_j = c + (j - 0.5)h$, $0 \le i \le N_x + 1$, $0 \le j \le N_y + 1$, where N_x and N_y are positive even integers and $h = (b - a)/N_x = (d - c)/N_y$ is the uniform mesh size. Then discrete domain and discrete boundary are defined as $\Omega^h = \{(x_i, y_j) | \ 1 \le i \le N_x, 1 \le j \le N_y\}$ and $\partial\Omega^h = \{(x_0, y_j), (x_{Nx+1}, y_j), (x_i, y_0), (x_i, y_{Ny+1}) | \ 1 \le i \le N_x, 1 \le j \le N_y\}$, respectively (see Fig. 2(b)). Note that the discrete boundary points are located at a half space step away from the true boundary points. It will be shown that this treatment of boundary points makes the solution algorithm be considerably simpler than standard treatments.

2.1. Discretization in a rectangular domain

Let ϕ_{ij}^n be an approximation of $\phi(x_i, y_j, n\Delta t)$, where $\Delta t = T/N_t$ is the time-step, T is the final time, and N_t is the total number of time-steps. We take $M \equiv 1$ for convenience. Then, a semi-implicit time and centered difference space discretization of the CH equation is given by

$$\frac{\phi_{ij}^{n+1} - \phi_{ij}^n}{\Delta t} = \Delta_d \mu_{ij}^{n+1}, \tag{7}$$

$$\mu_{ij}^{n+1} = F'(\phi_{ij}^{n+1}) + \phi_{ij}^{n+1} - \phi_{ij}^n - \epsilon^2 \Delta_d \phi_{ij}^{n+1}. \tag{8}$$

Here, the discrete Laplacian operator is defined by $\Delta_d \phi_{ij} = (\phi_{i+1,j} + \phi_{i-1,j} - 4\phi_{ij} + \phi_{i,j+1} + \phi_{i,j-1})/h^2$. The discrete boundary condition is defined as

$$\phi_{0j}^n = g(a, y_j), \qquad \phi_{N_x+1,j}^n = g(b, y_j), \qquad \phi_{i0}^n = g(x_i, c), \qquad \phi_{i,N_y+1}^n = g(x_i, d).$$

The resulting nonlinear system of Eqs. (7) and (8) is solved efficiently using a nonlinear multigrid method. The unconditionally gradient stability of the discrete system is proved in [53–56]. We define the discrete energy functional:

$$\mathcal{E}_h(\phi^n) = \sum_{i=1}^{N_x} \sum_{j=1}^{N_y} \left[h^2 F(\phi_{ij}^n) + \frac{\epsilon^2}{2} \left((\phi_{i+1,j}^n - \phi_{ij}^n)^2 + (\phi_{i,j+1}^n - \phi_{ij}^n)^2 \right) \right].$$

$\mathcal{E}_h(\phi^n)/\mathcal{E}_h(\phi^0)$ is defined as the normalized discrete total energy. We also define the discrete average mass as $\sum_{i=1}^{N_x} \sum_{j=1}^{N_y} \phi_{ij}^n/(N_x N_y)$. In [53,54], Eyre proved that if ϕ^{n+1} is a numerical solution of Eqs. (7) and (8) with a given ϕ^n, then $\mathcal{E}_h(\phi^{n+1}) \le \mathcal{E}_h(\phi^n)$. The decrease of the discrete total energy functional implies the pointwise boundedness of the numerical solution (please refer to [56] for more details and proof).

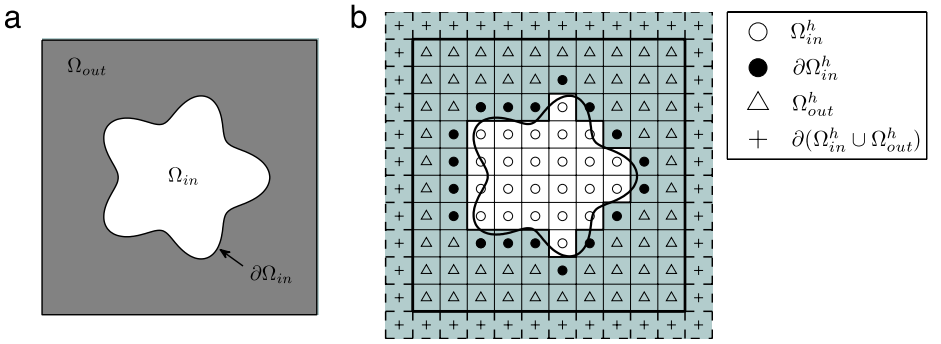

Fig. 3. (a) Complex domain Ω_{in} and (b) discrete complex domain Ω^h_{in}.

2.2. Conservation of the total mass in a rectangular domain

To satisfy the mass conservation property, i.e., $\sum_{i=1}^{N_x}\sum_{j=1}^{N_y}\phi_{ij}^{n+1} = \sum_{i=1}^{N_x}\sum_{j=1}^{N_y}\phi_{ij}^{n}$, we should have

$$\begin{aligned}
0 &= \sum_{i=1}^{N_x}\sum_{j=1}^{N_y}\frac{\phi_{ij}^{n+1}-\phi_{ij}^{n}}{\Delta t} = \sum_{i=1}^{N_x}\sum_{j=1}^{N_y}\Delta_d\mu_{ij}^{n+1}\\
&= \sum_{j=1}^{N_y}\sum_{i=1}^{N_x}\left(\frac{\mu_{i+1,j}^{n+1}-\mu_{ij}^{n+1}}{h^2}-\frac{\mu_{ij}^{n+1}-\mu_{i-1,j}^{n+1}}{h^2}\right)+\sum_{i=1}^{N_x}\sum_{j=1}^{N_y}\left(\frac{\mu_{i,j+1}^{n+1}-\mu_{ij}^{n+1}}{h^2}-\frac{\mu_{ij}^{n+1}-\mu_{i,j-1}^{n+1}}{h^2}\right)\\
&= \sum_{j=1}^{N_y}\left(\frac{\mu_{N_x+1,j}^{n+1}-\mu_{N_xj}^{n+1}}{h^2}-\frac{\mu_{1j}^{n+1}-\mu_{0j}^{n+1}}{h^2}\right)+\sum_{i=1}^{N_x}\left(\frac{\mu_{i,N_y+1}^{n+1}-\mu_{iN_y}^{n+1}}{h^2}-\frac{\mu_{i1}^{n+1}-\mu_{i0}^{n+1}}{h^2}\right),
\end{aligned}$$

where we have used Eq. (7) and telescoping cancellation. Therefore, if we impose the following numerical no-flux boundary conditions:

$$\begin{aligned}
&\mu_{0j}^{n+1}=\mu_{1j}^{n+1}, \qquad \mu_{N_x+1,j}^{n+1}=\mu_{N_xj}^{n+1} \quad \text{for } 1\le j\le N_y,\\
&\mu_{i0}^{n+1}=\mu_{i1}^{n+1}, \qquad \mu_{i,N_y+1}^{n+1}=\mu_{iN_y}^{n+1} \quad \text{for } 1\le i\le N_x,
\end{aligned}$$

then we have the mass conserving property.

2.3. Discretization in a complex domain

Next, we present a conservative discretization for the CH equation in a non-rectangular domain with Dirichlet boundary conditions. Let Ω_{in} be an arbitrarily shaped open domain embedded in Ω (see Fig. 3(a)). Also, let Ω^h_{in} be a discrete domain, $\partial\Omega^h_{\text{in}}$ be its discrete boundary, and $\Omega^h_{\text{out}} = \Omega^h \setminus (\Omega^h_{\text{in}} \cup \partial\Omega^h_{\text{in}})$ (see Fig. 3(b)).

As we refine the mesh, i.e., $h \to 0$, the arbitrarily shaped domain Ω_{in} is approximated by Ω^h_{in} (see Fig. 4).

To solve the CH equation in an arbitrarily shaped domain Ω_{in}, we propose the following numerical scheme:

$$\frac{\phi_{ij}^{n+1}-\phi_{ij}^{n}}{\Delta t} = G_{ij}^h\Delta_d\mu_{ij}^{n+1}, \tag{9}$$

$$\mu_{ij}^{n+1} = G_{ij}^h(F'(\phi_{ij}^{n+1})+\phi_{ij}^{n+1}-\phi_{ij}^{n}-\epsilon^2\Delta_d\phi_{ij}^{n+1})+\tilde{\mu}_{ij}^{n+1}. \tag{10}$$

Note that for $(x_i, y_j) \in \partial\Omega^h_{\text{in}}$, $\tilde{\mu}_{ij}^{n+1}$ will be defined in Section 2.4 and otherwise we assume $\tilde{\mu}_{ij}^{n+1} = 0$. The boundary control function G_{ij}^h is defined as

$$G_{ij}^h = G^h(x_i,y_j) = \begin{cases} 1 & \text{if } (x_i,y_j)\in\Omega^h_{\text{in}},\\ 0 & \text{if } (x_i,y_j)\in\Omega^h_{\text{out}}\cup\partial\Omega^h_{\text{in}}.\end{cases}$$

The discrete boundary condition is defined on the discrete boundary $\partial\Omega^h_{\text{in}}$ as $\phi_{ij}^n = g(x,y)$, where $(x,y) \in \partial\Omega$ and $|(x-x_i, y-y_j)| = \min_{(\alpha,\beta)\in\partial\Omega}|(\alpha-x_i,\beta-y_j)|$. Thus, by using the boundary control function G_{ij}^h, we can solve the CH equation in the arbitrarily shaped domain Ω^h_{in} as follows:

$$\frac{\phi_{ij}^{n+1}-\phi_{ij}^{n}}{\Delta t} = \begin{cases}\Delta_d\mu_{ij}^{n+1} & \text{if } (x_i,y_j)\in\Omega^h_{\text{in}},\\ 0 & \text{if } (x_i,y_j)\in\Omega^h_{\text{out}}\cup\partial\Omega^h_{\text{in}},\end{cases}$$

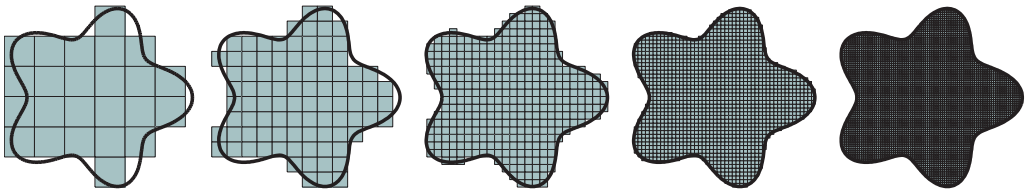

Fig. 4. Convergence of Ω_{in}^h to Ω_{in} as we refine the mesh.

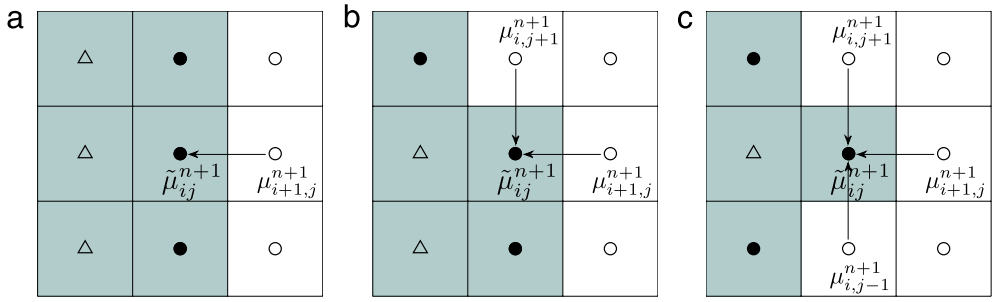

Fig. 5. Examples of discrete boundary point μ_{ij}^{n+1} in a complex domain. Each equation corresponding to each label is defined in Eq. (12).

$$\mu_{ij}^{n+1} = \begin{cases} F'(\phi_{ij}^{n+1}) + \phi_{ij}^{n+1} - \phi_{ij}^{n} - \epsilon^2 \Delta_d \phi_{ij}^{n+1} & \text{if } (x_i, y_j) \in \Omega_{\text{in}}^h, \\ \tilde{\mu}_{ij}^{n+1} & \text{if } (x_i, y_j) \in \partial\Omega_{\text{in}}^h, \\ 0 & \text{if } (x_i, y_j) \in \Omega_{\text{out}}^h. \end{cases}$$

2.4. Conservation of the total mass in a complex domain

In order to keep the conservation property for the CH equation in a complex domain Ω_{in}^h, i.e., $\sum_{(x_i,y_j)\in\Omega_{\text{in}}^h} (\phi_{ij}^{n+1} - \phi_{ij}^{n}) = 0$, we have to satisfy the following condition for $(x_i, y_j) \in \partial\Omega_{\text{in}}^h$:

$$\tilde{\mu}_{ij}^{n+1} = \frac{G_{i+1,j}^h \mu_{i+1,j}^{n+1} + G_{i-1,j}^h \mu_{i-1,j}^{n+1} + G_{i,j+1}^h \mu_{i,j+1}^{n+1} + G_{i,j-1}^h \mu_{i,j-1}^{n+1}}{G_{i+1,j}^h + G_{i-1,j}^h + G_{i,j+1}^h + G_{i,j-1}^h}. \tag{11}$$

Note that $G_{i+1,j}^h + G_{i-1,j}^h + G_{i,j+1}^h + G_{i,j-1}^h$ is always positive for $(x_i, y_j) \in \partial\Omega_{\text{in}}^h$. Therefore, $\tilde{\mu}_{ij}^{n+1}$ is well-defined. Fig. 5 represents examples of $\tilde{\mu}_{ij}^{n+1}$:

$$\begin{cases} \text{(a) } \tilde{\mu}_{ij}^{n+1} = \mu_{i+1,j}^{n+1}, \\ \text{(b) } \tilde{\mu}_{ij}^{n+1} = (\mu_{i+1,j}^{n+1} + \mu_{i,j+1}^{n+1})/2, \quad \text{and} \\ \text{(c) } \tilde{\mu}_{ij}^{n+1} = (\mu_{i+1,j}^{n+1} + \mu_{i,j+1}^{n+1} + \mu_{i,j-1}^{n+1})/3. \end{cases} \tag{12}$$

Let us define four types of boundaries as

$$\begin{aligned} \partial\Omega_{\text{in},l}^h &= \{(x_i, y_j) \in \partial\Omega_{\text{in}}^h \mid (x_{i+1}, y_j) \in \Omega_{\text{in}}^h\}, \\ \partial\Omega_{\text{in},r}^h &= \{(x_i, y_j) \in \partial\Omega_{\text{in}}^h \mid (x_{i-1}, y_j) \in \Omega_{\text{in}}^h\}, \\ \partial\Omega_{\text{in},b}^h &= \{(x_i, y_j) \in \partial\Omega_{\text{in}}^h \mid (x_i, y_{j+1}) \in \Omega_{\text{in}}^h\}, \\ \partial\Omega_{\text{in},t}^h &= \{(x_i, y_j) \in \partial\Omega_{\text{in}}^h \mid (x_i, y_{j-1}) \in \Omega_{\text{in}}^h\}. \end{aligned}$$

Then $\partial\Omega_{\text{in}}^h = \partial\Omega_{\text{in},l}^h \cup \partial\Omega_{\text{in},r}^h \cup \partial\Omega_{\text{in},b}^h \cup \partial\Omega_{\text{in},t}^h$. These definitions are illustrated in Fig. 6.

Now, we will prove the mass conservation property of our proposed scheme on a discrete complex domain. By summing Eq. (9) in the complex numerical domain, Ω_{in}^h, we get

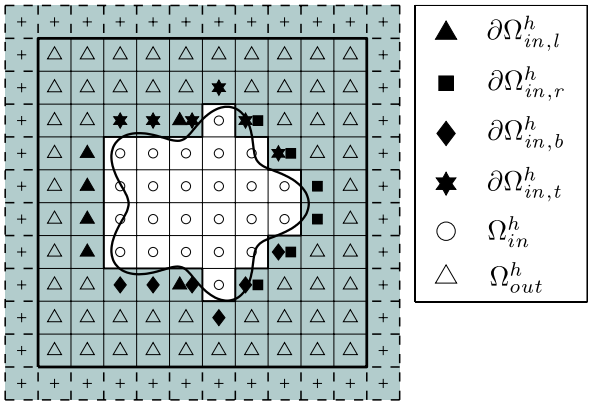

Fig. 6. Complex domain with different boundaries.

$$
\begin{aligned}
\sum_{(x_i,y_j)\in\Omega^h_{\text{in}}} \frac{\phi^{n+1}_{ij}-\phi^n_{ij}}{\Delta t} &= \sum_{(x_i,y_j)\in\Omega^h_{\text{in}}} \Delta_d \mu^{n+1}_{ij} \\
&= \sum_{(x_i,y_j)\in\partial\Omega^h_{\text{in},r}} \frac{\tilde{\mu}^{n+1}_{ij}-\mu^{n+1}_{i-1,j}}{h^2} - \sum_{(x_i,y_j)\in\partial\Omega^h_{\text{in},l}} \frac{\mu^{n+1}_{i+1,j}-\tilde{\mu}^{n+1}_{ij}}{h^2} \\
&\quad + \sum_{(x_i,y_j)\in\partial\Omega^h_{\text{in},t}} \frac{\tilde{\mu}^{n+1}_{ij}-\mu^{n+1}_{i,j-1}}{h^2} - \sum_{(x_i,y_j)\in\partial\Omega^h_{\text{in},b}} \frac{\mu^{n+1}_{i,j+1}-\tilde{\mu}^{n+1}_{ij}}{h^2} \\
&= \sum_{(x_i,y_j)\in\partial\Omega^h_{\text{in}}} \Bigg[\frac{G^h_{i-1,j}(\tilde{\mu}^{n+1}_{ij}-\mu^{n+1}_{i-1,j}) - G^h_{i+1,j}(\mu^{n+1}_{i+1,j}-\tilde{\mu}^{n+1}_{ij})}{h^2} \\
&\quad + \frac{G^h_{i,j-1}(\tilde{\mu}^{n+1}_{ij}-\mu^{n+1}_{i,j-1}) - G^h_{i,j+1}(\mu^{n+1}_{i,j+1}-\tilde{\mu}^{n+1}_{ij})}{h^2} \Bigg] \\
&= \sum_{(x_i,y_j)\in\partial\Omega^h_{\text{in}}} \Bigg[\frac{(G^h_{i+1,j}+G^h_{i-1,j}+G^h_{i,j+1}+G^h_{i,j-1})\tilde{\mu}^{n+1}_{ij}}{h^2} \\
&\quad - \frac{G^h_{i+1,j}\mu^{n+1}_{i+1,j}+G^h_{i-1,j}\mu^{n+1}_{i-1,j}+G^h_{i,j+1}\mu^{n+1}_{i,j+1}+G^h_{i,j-1}\mu^{n+1}_{i,j-1}}{h^2} \Bigg] = 0,
\end{aligned}
$$

where we have used Eq. (11) in the last equality. Therefore, we have proved the mass conservation property of the proposed numerical scheme for the CH equation with Dirichlet boundary conditions in complex domains.

2.5. Nonlinear multigrid solver in a complex domain

In this section, we use a nonlinear full approximation storage multigrid method to solve the nonlinear discrete system (9) and (10) at the implicit time level. To condense the discussion we describe only the relaxation step of the method. First, rewrite Eqs. (9) and (10) as follows:

$$
\begin{aligned}
&\frac{\phi^{n+1}_{ij}}{\Delta t} + \frac{4G^h_{ij}\mu^{n+1}_{ij}}{h^2} = \frac{\phi^n_{ij}}{\Delta t} + G^h_{ij}\frac{\mu^{n+1}_{i+1,j}+\mu^{n+1}_{i-1,j}+\mu^{n+1}_{i,j+1}+\mu^{n+1}_{i,j-1}}{h^2}, \\
&-\frac{4G^h_{ij}\epsilon^2}{h^2}\phi^{n+1}_{ij} - G^h_{ij}(\phi^{n+1}_{ij})^3 + \mu^{n+1}_{ij} = -G^h_{ij}\phi^n_{ij} - \frac{G^h_{ij}\epsilon^2}{h^2}(\phi^{n+1}_{i+1,j}+\phi^{n+1}_{i-1,j}+\phi^{n+1}_{i,j+1}+\phi^{n+1}_{i,j-1}) + \tilde{\mu}^{n+1}_{ij}.
\end{aligned}
$$

Next, we replace ϕ^{n+1}_{kl} and μ^{n+1}_{kl} in the above equations with $\bar{\phi}^m_{kl}$ and $\bar{\mu}^m_{kl}$ if $k \le i$ and $l \le j$, otherwise with ϕ^m_{kl} and μ^m_{kl}, i.e.,

$$
\begin{aligned}
&\frac{\bar{\phi}^m_{ij}}{\Delta t} + \frac{4G^h_{ij}\bar{\mu}^m_{ij}}{h^2} = \frac{\phi^n_{ij}}{\Delta t} + G^h_{ij}\frac{\mu^m_{i+1,j}+\bar{\mu}^m_{i-1,j}+\mu^m_{i,j+1}+\bar{\mu}^m_{i,j-1}}{h^2}, \\
&-\frac{4G^h_{ij}\epsilon^2}{h^2}\bar{\phi}^m_{ij} - G^h_{ij}(\bar{\phi}^m_{ij})^3 + \bar{\mu}^m_{ij} = -G^h_{ij}\phi^n_{ij} - \frac{G^h_{ij}\epsilon^2}{h^2}(\phi^m_{i+1,j}+\bar{\phi}^m_{i-1,j}+\phi^m_{i,j+1}+\bar{\phi}^m_{i,j-1}) + \tilde{\mu}^m_{ij}.
\end{aligned} \tag{13}
$$

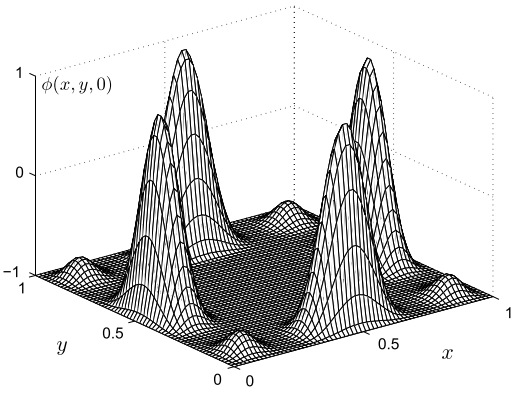

Fig. 7. Initial condition $\phi(x, y, 0)$ on Ω_{in}.

Since $(\bar{\phi}_{ij}^m)^3$ in Eq. (13) is nonlinear with respect to $\bar{\phi}_{ij}^m$, we linearize $(\bar{\phi}_{ij}^m)^3$ at ϕ_{ij}^m:

$$(\bar{\phi}_{ij}^m)^3 = (\phi_{ij}^m)^3 + 3(\phi_{ij}^m)^2(\bar{\phi}_{ij}^m - \phi_{ij}^m).$$

After substituting this expression into Eq. (13), we obtain

$$-G_{ij}^h\left(\frac{4\epsilon^2}{h^2} + 3(\phi_{ij}^m)^2\right)\bar{\phi}_{ij}^m + \bar{\mu}_{ij}^m = \psi_{ij}^n - G_{ij}^h\frac{\epsilon^2}{h^2}\left(\phi_{i+1,j}^m + \bar{\phi}_{i-1,j}^m + \phi_{i,j+1}^m + \bar{\phi}_{i,j-1}^m\right) - 2G_{ij}^h(\phi_{ij}^m)^3 + \tilde{\mu}_{ij}^m. \tag{14}$$

It should be noticed that for the boundary point $(x_i, y_j) \in \partial\Omega_{\text{in}}^h$, we use Eq. (11) as

$$\tilde{\mu}_{ij}^m = \frac{G_{i+1,j}^h\mu_{i+1,j}^m + G_{i-1,j}^h\bar{\mu}_{i-1,j}^m + G_{i,j+1}^h\mu_{i,j+1}^m + G_{i,j-1}^h\bar{\mu}_{i,j-1}^m}{G_{i+1,j}^h + G_{i-1,j}^h + G_{i,j+1}^h + G_{i,j-1}^h}.$$

For restriction and interpolation operators, we briefly describe them here. For more details, please refer to [17].

3. Numerical results

In this section, we perform the following numerical experiments: a convergence test, a test of the stability of the proposed scheme, a comparison of Dirichlet and Neumann boundary conditions for spinodal decompositions, and their effects on the increasing area in rectangular and complex domains, applications of models for biological membranes in confined domains, and a passively moving droplet in a wavy channel.

Unless otherwise specified, a 128 × 128 mesh grid is used on the computational domain $\Omega = (0, 1) \times (0, 1)$ and $\Delta t = 0.2h$ is used for the time integration. Furthermore, across the interfacial regions, the concentration field varies from -0.9 to 0.9 over a distance of approximately $2\sqrt{2}\epsilon \tanh^{-1}(0.9)$. Therefore, if we want this value to be approximately m grid points, the ϵ value needs to be taken as follows: $\epsilon_m = hm/[2\sqrt{2}\tanh^{-1}(0.9)]$. In our numerical simulation, we set $\epsilon = \epsilon_8$.

3.1. Convergence test

We start with spatial and temporal convergence tests of the proposed method. In order to obtain the spatial convergence rate, we perform a number of simulations with increasingly finer grids $h = 1/2^{n-1}$ for $n = 6, 7$, and 8 on a computational domain $\Omega_{\text{in}} = (-1, 1) \times (-1, 1) \setminus [-0.5, 0.5] \times [-0.5, 0.5]$. We define the function $f(x, y) = (x^2 - 1)(x^2 - 0.25)(y^2 - 1)(y^2 - 0.25)$. The initial condition is $\phi(x, y, 0) = 2f^4/\|f^4\|_\infty - 1$ where $\|f\|_\infty$ is the maximum of f on the domain Ω_{in}, shown in Fig. 7. The minus one Dirichlet boundary condition, i.e., $g(\mathbf{x}) = -1$ and $\epsilon = 0.0113$ are used. Numerical solutions are computed up to time $T = 0.0001$.

Since there is no closed-form analytical solution for this problem, we consider a reference numerical solution, ϕ^{ref}, which is obtained with very fine spatial and temporal grids. In this test, we use a 1024 × 1024 mesh grid and $\Delta t = 6.25\text{E}{-6}$. We define the error of a grid as the discrete l_2-norm of the difference between that grid and the average of the reference solution cells neighboring it as follows: $e_{hij} := \phi_{hij} - (\phi_{p-1,q-1}^{\text{ref}} + \phi_{p,q-1}^{\text{ref}} + \phi_{p-1,q}^{\text{ref}} + \phi_{pq}^{\text{ref}})/4$. Here, p and q are appropriate fine reference grid indexes. The rate of convergence is defined as the ratio of successive errors: $\log_2(\|e_h\|_2/\|e_{\frac{h}{2}}\|_2)$. The errors and rates of convergence obtained using these definitions are given in Table 1. Second-order accuracy with respect to space is observed, as expected from the discretization.

To obtain the convergence rate for temporal discretization, we fix the space step size as $h = 1/128$ and choose a set of decreasing time-steps $\Delta t = 6.25\text{E}{-4}$, $3.125\text{E}{-4}$ and $1.563\text{E}{-4}$. Numerical solutions are computed up to time $T = 0.005$. Note that in this test we define the l_2-norm error of a grid to be $e_{\Delta t\,ij} := \phi_{\Delta t\,ij} - \phi_{ij}^{\text{ref}}$. Here, ϕ^{ref} is the reference numerical solution which is obtained with a small time-step $\Delta t = 1.953\text{E}{-5}$. The errors and rates of convergence obtained using these definitions are given in Table 2. First-order accuracy with respect to time is observed, as expected from the discretization.

Table 1
Error and convergence results with various mesh grids. Here, $\Delta t = 6.25\text{E}{-6}$.

Grid	64×64		128×128		256×256
l_2-error	3.90E−3		8.92E−4		2.07E−4
Rate		2.13		2.11	

Table 2
Error and convergence results with various time-steps. Here, a 256×256 mesh grid is used.

Δt	6.25E−4		3.125E−4		1.563E−4
l_2-error	3.30E−2		1.61E−2		7.21E−3
Rate		1.03		1.16	

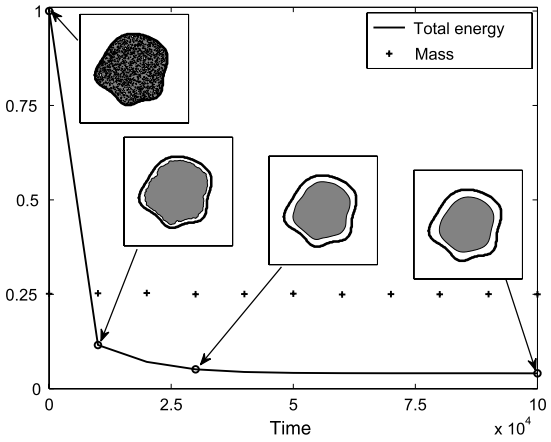

Fig. 8. Temporal evolution with large time-step $\Delta t = 10\,000$.

3.2. Stability of the proposed scheme

The proposed scheme (9) and (10) with Dirichlet boundary conditions is unconditionally gradient stable. In order to demonstrate this, we perform a numerical experiment in a complex domain with a large time-step, $\Delta t = 10\,000$. The initial condition is random perturbations with a maximum amplitude of 0.75, that is, $\phi(x, y, 0) = 0.25 + 0.75\text{rand}(x, y)$, where $\text{rand}(x, y)$ is a random number between -1 and 1. The numerical solutions are obtained from 10 iterations and are shown in Fig. 8, which represents the non-increasing discrete total energy and conservation of mass concentration of the numerical solutions with large time-step. These results suggest that our proposed scheme with the Dirichlet boundary condition is indeed unconditionally stable.

3.3. Spinodal decomposition with Dirichlet and Neumann boundary conditions

We perform a numerical experiment with an example of spinodal decomposition of a binary mixture. Spinodal decomposition is a mechanism by which a solution of two or more components separates into different phases. The system separates into spatial regions rich in one species and poor in the other species and evolves into an equilibrium state with a lower overall free energy [1]. Here, we will consider this problem for the CH equation using a minus one Dirichlet boundary, i.e., $g(\mathbf{x}) = -1$ and the Neumann boundary with the initial condition $\phi(x, y, 0) = 0.25 + 0.75\text{rand}(x, y)$. Simulations are run up to time $T = 7.81$. Fig. 9(a) and (b) show the evolutions of spinodal decomposition with Dirichlet and Neumann boundary conditions, respectively. With the minus one Dirichlet boundary condition, the positive phases are gathered away from the boundary. With the Neumann boundary, the phases keep the 90° contact angle on the boundary. More detailed models and simulations of the contact angle in phase-fields are described in [57]. From Fig. 9(c), we observe that the average composition is preserved and the total discrete energy is non-increasing.

We also consider spinodal decomposition with variable Dirichlet boundary conditions. The control function $G(x, y)$ and initial configuration $\phi(x, y, 0)$ are defined as

$$G(x, y) = \begin{cases} 0, & \text{if } \sqrt{(x-0.5)^2 + (y-0.5)^2} > 0.3 + 0.1\sin(7\theta), \\ 1, & \text{otherwise.} \end{cases} \tag{15}$$

$$\phi(x, y, 0) = \begin{cases} -\sin(3(\theta+\pi)^2/\pi), & \text{if } (x, y) \in \partial\Omega_{\text{in}}, \\ 0.55 + 0.75\text{rand}(x, y), & \text{if } (x, y) \in \Omega_{\text{in}}, \end{cases} \tag{16}$$

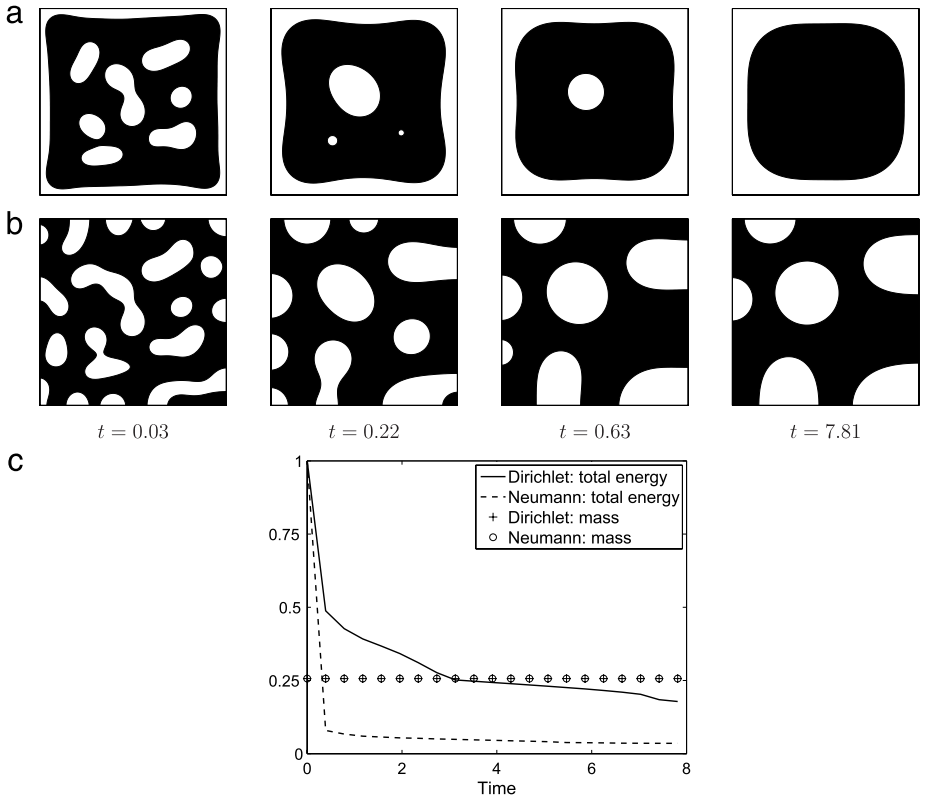

Fig. 9. Evolutions with (a) Dirichlet and (b) Neumann boundary conditions. Evolution times are given below each figure. (c) The non-increasing discrete total energy and conservation of mass concentration of the numerical solutions.

where

$$\theta = \begin{cases} \tan^{-1}\left(\dfrac{y-0.5}{x-0.5}\right), & \text{if } x > 0.5, \\ \pi + \tan^{-1}\left(\dfrac{y-0.5}{x-0.5}\right), & \text{otherwise.} \end{cases} \tag{17}$$

In Fig. 10(a), we show that the boundary condition $g(x, y) = -\sin(3(\theta + \pi)^2/\pi)$ by a stem plot. Using this boundary condition, the evolution of spinodal decomposition is shown in Fig. 10(b)–(e). The computational times are shown below each figure. Results in Fig. 10 suggest that our proposed method works well with the variable Dirichlet boundary condition.

3.4. Effects of Dirichlet and Neumann boundary conditions on increasing area

In order to further investigate the effects of the Dirichlet boundary condition, we consider growing phases inside a confined domain. To increase the area, we add a source term $F(\phi) = 0.25(\phi^2 - 1)^2$ to the CH equation, such that

$$\frac{\partial \phi}{\partial t} = \Delta \mu + \lambda F(\phi), \tag{18}$$

where λ is a constant and depending on its sign the average concentration of the phase increases or decreases. This type of source term has been used in simulating crystal growth [58–60] and solving image segmentation problems [61]. We solve Eq. (18) with Dirichlet and Neumann boundary conditions using the same initial condition

$$\phi(x, y, 0) = \tanh\left(\frac{0.3 - \sqrt{(x-0.5)^2 + (y-0.5)^2}}{\sqrt{2}\epsilon}\right).$$

Here, we use $\lambda = 50$ to make the phases grow until the average composition of the phases becomes 0.7. We then set $\lambda = 0$ until $t = 2.34$ when the phases converge to a numerical steady state. These evolutions are shown in Fig. 11(a) and (b) for Dirichlet and Neumann boundary conditions, respectively. Fig. 11(c) shows the time-dependent non-dimensional

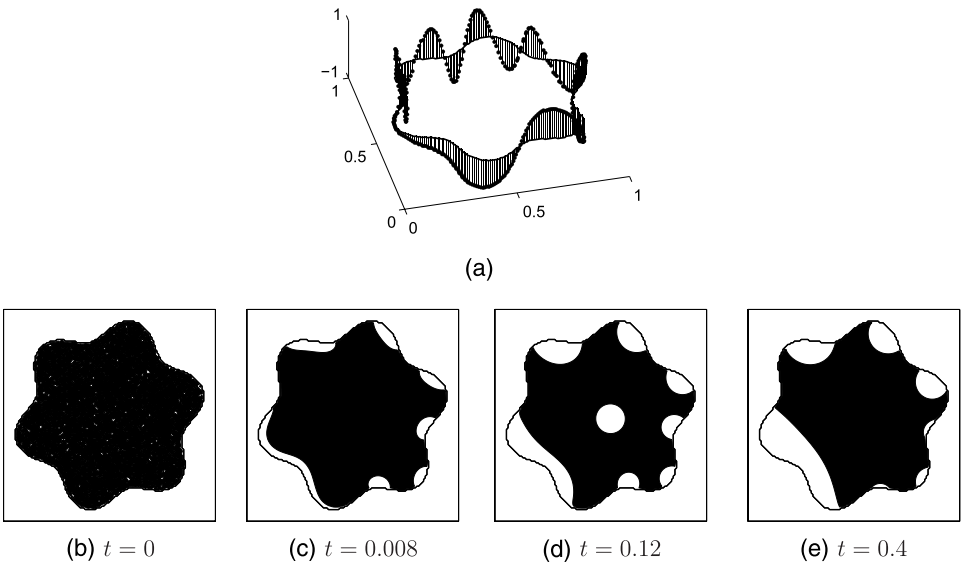

Fig. 10. (a) Plot of the boundary condition $g(x, y) = -\sin(3(\theta + \pi)^2/\pi)$. (b)–(e) Evolution of spinodal decomposition. The computational times are shown below each figure.

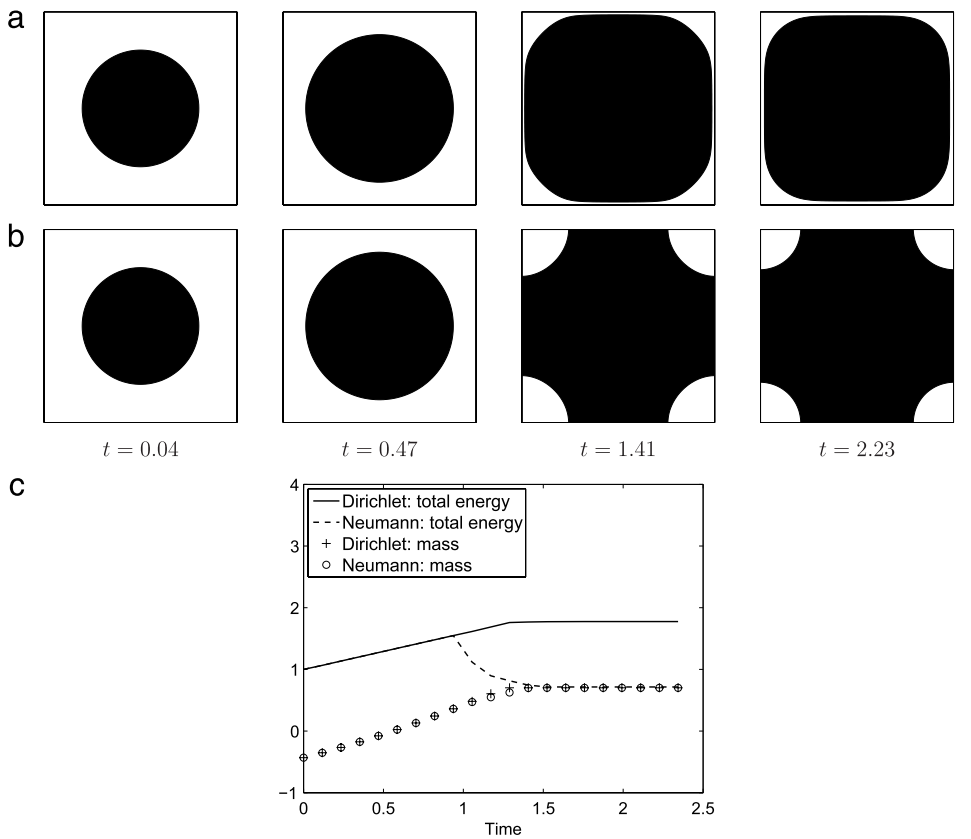

Fig. 11. Evolutions with (a) Dirichlet and (b) Neumann boundary conditions. Evolution times are given below each figure. (c) Evolution of the total energy and average mass.

discrete total energy and mass change of the numerical solution. From the evolutions with two boundary conditions, it can be observed that when the Dirichlet boundary condition is used, the interface does not wet the domain boundary. On the other hand, for the Neumann boundary condition, the phases wet the boundary and is in contact with it by 90°.

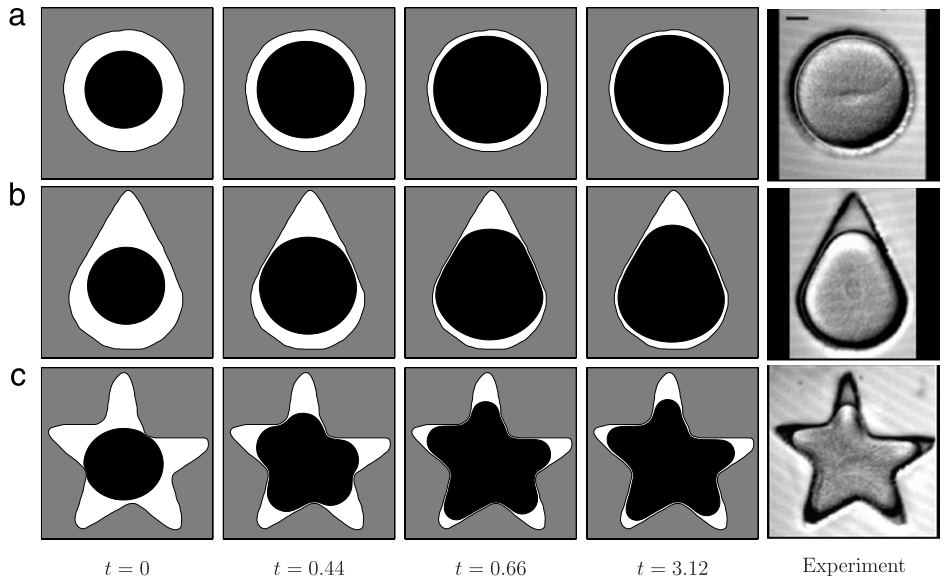

Fig. 12. Evolution of cell growth in confined domains. From left to right, first column: initial configurations; second and third columns: cell growth results; fourth column: steady cell shapes with doubled cell area; and last column: figures reprinted with permission from Minc et al., Cell, **144**, 414–426 (2011) [52].
© 2011, Elsevier.

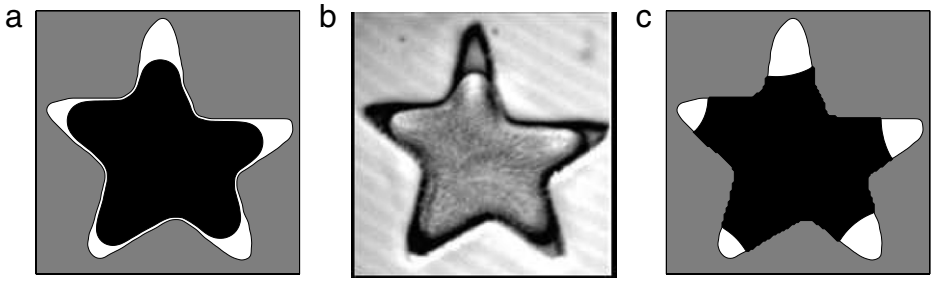

Fig. 13. (a) and (c) are steady states with Dirichlet and Neumann boundary conditions, respectively; (b) figure reprinted with permission from Minc et al., Cell, **144**, 414–426 (2011) [52].
© 2011, Elsevier.

3.5. Application of models for biological membrane in confined domains

One application of phase-field models with Dirichlet boundary conditions is modeling biological membranes in confined domains. As an example, we consider sea urchin embryos placed in microfabricated chambers for an investigation of how cell shape affects the positioning of the nucleus, spindle, and subsequent cell division planes [52]. The last column in Fig. 12 shows differential interference contrast (DIC) pictures of eggs in the chambers adopting different geometries in real experiments.

To simulate numerically these experimental results, we set initial configurations on confined domains as shown in the first column in Fig. 12 and we give $\lambda = 50$ in Eq. (18) to make the cell grow until the cell doubles in its area. Once the cell doubles in its area, we reset $\lambda = 0$ to stop the cell growth, and then we run the simulation until a numerical solution reaches a steady state. From the second column to the fourth column, we show the evolution in each case. These results show that our computational results are in good qualitative agreement with the experimental data. Unlike the Neumann boundary condition, the Dirichlet boundary condition allows us to model membrane dynamics in confined domains with relatively coarse grids (see Fig. 13(a)). Note that if we had used the Neumann boundary condition, then cell membranes would have been broken and become attached to the wall as shown in Fig. 13(c).

3.6. A passively moving droplet in a wavy channel

Fig. 14 shows the droplet evolution in the given flow field at $t = 0$, 1.22, 1.83, 2.44, 3.66, and 4.88 from top to bottom. The channel geometry is given by two sine functions with period 2 and amplitude 0.25. The vertical distance between the boundaries is 0.4 and the channel domain is embedded in the computational domain $\Omega = (0, 5) \times (0, 1)$ with a 320×64

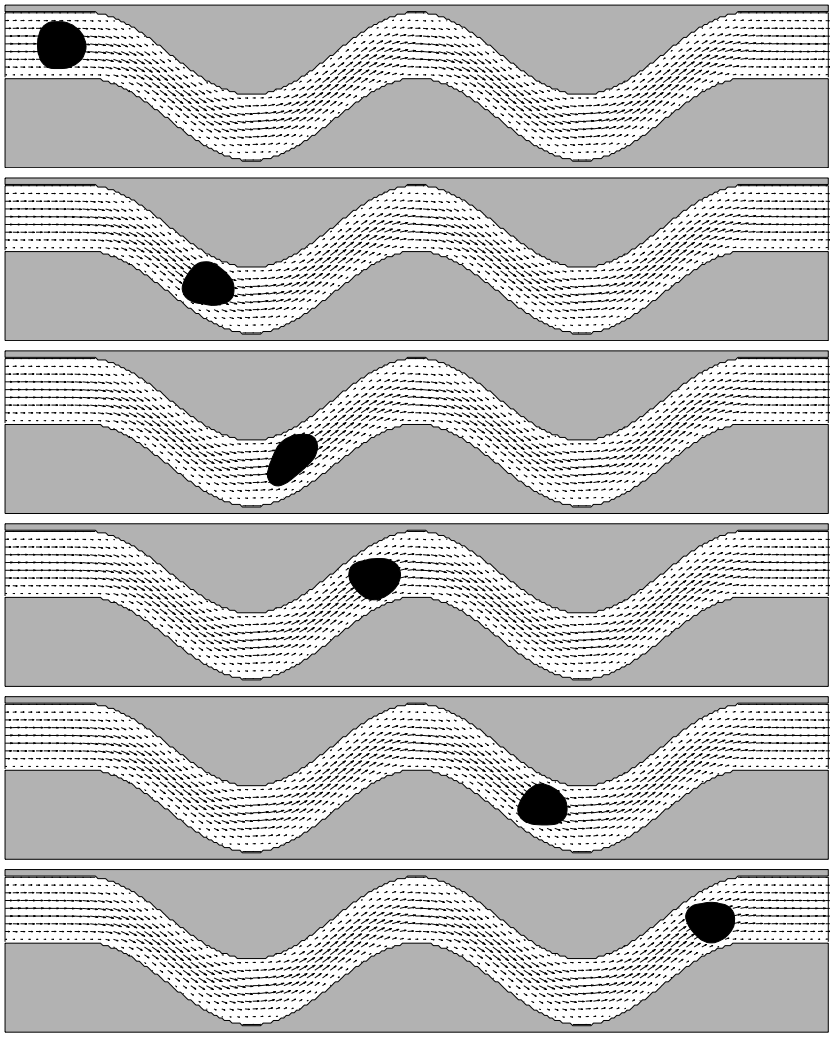

Fig. 14. Droplet evolutions in the flow velocity field with a wavy channel.

mesh grid. Initially, the droplet of diameter 0.3 is placed at the upper left. At the inflow, we use a parabolic velocity profile, $(-24(y-0.55)(y-0.95), 0)$. Similar numerical experiments were performed to simulate two-phase flows with complex geometries using adaptive finite elements [30]. In [30], the droplet evolution was simulated over time by the flow field in a wavy channel with a boundary condition that encodes the contact line information. Our proposed method applies the Dirichlet boundary condition to prevent contact between the droplet and the channel. The flow vector field is driven by the Navier–Stokes equation with the no-slip Dirichlet boundary condition and with a Reynolds number of 1, and the droplet is moved by evolving the advective CH equation. In this simulation, the droplet is transported passively by the given background velocity field. As the droplet moves through the channel, it is deformed as a result of the given velocity field.

4. Conclusions

In this paper we presented a conservative numerical method for the Cahn–Hilliard equation with Dirichlet boundary conditions in complex domains. The method used an unconditionally gradient stable nonlinear splitting numerical scheme to remove the high-order time-step stability constraints. The resulting discrete equations were solved by a nonlinear multigrid method. We described the implementation of our numerical scheme in more detail. A continuous problem had mass conservation and it was proved that this property holds for a discrete problem. We numerically showed the total energy decrease and the unconditionally gradient stability. We demonstrated the accuracy and robustness of the proposed Dirichlet boundary formulation with various numerical experiments. The numerical results showed the potential usefulness of the proposed method for accurately calculating membrane dynamics in confined domains. In the future work, we will compare our proposed method with other numerical methods, for example, adaptive finite element method [30] and apply our method to simulate biological membrane dynamics in confined domains.

Acknowledgments

This research was supported by the Basic Science Research Program through the National Research Foundation of Korea (NRF) funded by the Ministry of Education, Science and Technology (No. 2011-0023794). The authors thank the reviewers for the constructive and helpful comments on the revision of this article.

References

[1] J.W. Cahn, On spinodal decomposition, Acta Metall. 9 (1961) 795–801.
[2] J.W. Cahn, J.E. Hilliard, Free energy of a nonuniform system. I: interfacial free energy, J. Chem. Phys. 28 (1958) 258–267.
[3] P.C. Fife, Models for phase separation and their mathematics, Electron. J. Differential Equations 2000 (2000) 1–26.
[4] S.M. Choo, S.K. Chung, K.I. Kim, Conservative nonlinear difference scheme for the Cahn–Hilliard equation II, Comput. Math. Appl. 39 (2000) 229–243.
[5] P.M. Dupuya, M. Fernandino, H.A. Jakobsen, H.F. Svendsena, Using Cahn–Hilliard mobility to simulate coalescence dynamics, Comput. Math. Appl. 59 (2010) 2246–2259.
[6] Q.-F. Wang, Optimal distributed control of nonlinear Cahn–Hilliard systems with computational realization, J. Math. Sci. 177 (2011) 440–458.
[7] M. Dehghan, D. Mirzaei, A numerical method based on the boundary integral equation and dual reciprocity methods for one-dimensional Cahn–Hilliard equation, Eng. Anal. Bound. Elem. 4 (2009) 522–528.
[8] V.E. Badalassi, H.D. Ceniceros, S. Banerjee, Computation of multiphase systems with phase field models, J. Comput. Phys. 190 (2003) 371–397.
[9] L. Baňnas, R. Nürnberg, A posteriori estimates for the Cahn–Hilliard equation with obstacle free energy, M2AN, Math. Model. Numer. Anal. 43 (2009) 1003–1026.
[10] L. Baňnas, R. Nürnberg, Adaptive finite element methods for Cahn–Hilliard equations, J. Comput. Appl. Math. 218 (2008) 2–11.
[11] D. Furihata, A stable and conservative finite difference scheme for the Cahn–Hilliard equation, Numer. Math. 87 (2001) 675–699.
[12] H. Garcke, B. Nestler, B. Stoth, A multiphase field concept: numerical simulations of moving phase boundaries and multiple junctions, SIAM J. Appl. Math. 60 (1999) 295–315.
[13] J. Kim, K. Kang, J. Lowengrub, Conservative multigrid methods for Cahn–Hilliard fluids, J. Comput. Phys. 193 (2004) 511–543.
[14] D. Kay, R. Welford, A multigrid finite element solver for the Cahn–Hilliard equation, J. Comput. Phys. 212 (2006) 288–304.
[15] A.G. Lamorgese, R. Mauri, Diffuse-interface modeling of phase segregation in liquid mixtures, Int. J. Multiph. Flow 3 (2008) 987–995.
[16] G.N. Wells, E. Kuhl, K. Garikipati, A discontinuous Galerkin method for the Cahn–Hilliard equation, J. Comput. Phys. 218 (2006) 860–877.
[17] J. Shin, D. Jeong, J. Kim, A conservative numerical method for the Cahn–Hilliard equation in complex domains, J. Comput. Phys. 230 (2011) 7441–7455.
[18] R. Choksi, M.A. Peletier, J.F. Williams, On the phase diagram for microphase separation of diblock copolymers: an approach via a nonlocal Cahn–Hilliard functional, SIAM J. Appl. Math. 69 (2009) 1712–1738.
[19] H.D. Ceniceros, A.M. Roma, A nonstiff, adaptive mesh refinement-based method for the Cahn–Hilliard equation, J. Comput. Phys. 225 (2007) 1849–1862.
[20] L.Q. Chen, J. Shen, Applications of semi-implicit Fourier-spectral method to phase-field equations, Comput. Phys. Comm. 108 (1998) 147–158.
[21] W.M. Feng, P. Yu, S.Y. Hu, Z.K. Liu, Q. Du, L.Q. Chen, Spectral implementation of an adaptive moving mesh method for phase-field equations, J. Comput. Phys. 220 (2006) 498–510.
[22] H. Gómez, V. Calo, Y. Bazilevs, T. Hughes, Isogeometric analysis of the Cahn–Hilliard phase field model, Comput. Methods Appl. Mech. Eng. 197 (2008) 4333–4352.
[23] L. He, Error estimation of a class of stable spectral approximation to the Cahn–Hilliard equation, J. Sci. Comput. 41 (2009) 461–482.
[24] Y. He, Y. Liu, T. Tang, On large time-stepping methods for the Cahn–Hilliard equation, Appl. Numer. Math. 57 (2007) 616–628.
[25] J. Shen, X. Yang, An efficient moving mesh spectral method for the phase-field model of two-phase flows, J. Comput. Phys. 228 (2009) 2978–2992.
[26] X. Ye, The Fourier collocation method for the Cahn–Hilliard equation, Comput. Math. Appl. 44 (2002) 213–229.
[27] M. Dehghan, R. Jazlanian, A high-order non-oscillatory central scheme with non-staggered grids for hyperbolic conservation laws, Comput. Phys. Comm. 182 (2011) 1284–1294.
[28] M. Dehghan, R. Jazlanian, A fourth-order central Runge–Kutta scheme for hyperbolic conservation laws, Numer. Methods Partial Differential Equations 26 (2010) 1675–1692.
[29] M. Dehghan, F. Fakhar-Izadi, The spectral collocation method with three different bases for solving a nonlinear partial differential equation arising in modeling of nonlinear waves, Math. Comput. Modelling 53 (2011) 1865–1877.
[30] S. Aland, J. Lowengrub, A. Voigt, Two-phase flow in complex geometries: a diffuse domain approach, Comput. Model. Eng. Sci. 57 (2010) 77–108.
[31] H. Ding, P.D.M. Spelt, Wetting condition in diffuse interface simulations of contact line motion, Phys. Rev. E 75 (2007) 046708.
[32] D. Jacqmin, Contact-line dynamics of a diffuse fluid interface, J. Fluid Mech. 402 (2000) 57–88.
[33] Q. Du, R.A. Nicolaides, Numerical analysis of a continuum model of phase transition, SIAM J. Numer. Anal. 28 (1991) 1310–1322.
[34] L. Bronsard, D. Hilhorst, On the slow dynamics for the Cahn–Hilliard equation in one space dimension, Proc. R. Soc. Lond. Ser. A 439 (1992) 669–682.
[35] P. Bates, J. Han, The Dirichlet boundary problem for a nonlocal Cahn–Hilliard equation, J. Math. Anal. Appl. 311 (2005) 289–312.
[36] M. Dehghan, A. Mohebbi, Multigrid solution of high order discretisation for three-dimensional biharmonic equation with Dirichlet boundary conditions of second kind, Appl. Math. Comput. 180 (2006) 575–593.
[37] M. Dehghan, Finite difference procedures for solving a problem arising in modeling and design of certain optoelectronic devices, Math. Comput. Simul. 71 (2006) 16–30.
[38] A. Shokri, M. Dehghan, A meshless method using the radial basis functions for numerical solution of the regularized long wave equation, Numer. Methods Partial Differential Equations 26 (2010) 807–825.
[39] Y. Liu, W.K. Liu, Rheology of red blood cell aggregation by computer simulation, J. Comput. Phys. 220 (2006) 139–154.
[40] W.K. Liu, Y. Liu, D. Farrell, L. Zhang, X.S. Wang, Y. Fukui, N. Patankar, Y. Zhang, C. Bajaj, J. Lee, J. Hong, X. Chen, H. Hsu, Immersed finite element method and its applications to biological systems, Comput. Methods Appl. Mech. Eng. 195 (2006) 1722–1749.
[41] J. Zhang, P.C. Johnson, A.S. Popel, Red blood cell aggregation and dissociation in shear flows simulated by lattice Boltzmann method, J. Biomech. 41 (2008) 47–55.
[42] C. Migliorini, Y. Qian, H. Chen, E.B. Brown, R.K. Jain, L.L. Munn, Red blood cells augment leukocyte rolling in a virtual blood vessel, Biophys. J. 83 (2002) 1834–1841.
[43] C. Sun, C. Migliorini, L.L. Munn, Red blood cells initiate leukocyte rolling in postcapillary expansions: a lattice Boltzmann analysis, Biophys. J. 85 (2003) 208–222.
[44] C. Sun, L.L. Munn, Particulate nature of blood determines macroscopic rheology: a 2-D lattice Boltzmann analysis, Biophys. J. 88 (2005) 1635–1645.
[45] R.M. MacMeccan, J.R. Clausen, G.P. Neitzel, C.K. Aidun, Simulating deformable particle suspensions using a coupled lattice-Boltzmann and finite element method, J. Fluid Mech. 618 (2009) 13–39.
[46] H. Zhao, A.H.G. Isfahani, L.N. Olson, J.B. Freund, A spectral boundary integral method for flowing blood cells, J. Comput. Phys. 229 (2010) 3726–3744.
[47] P. Bagchi, P.C. Johnson, A.S. Popel, Computational fluid dynamic simulation of aggregation of deformable cells in a shear flow, J. Bio. Eng. 127 (2005) 1070–1080.
[48] C.D. Eggleton, A.S. Popel, Large deformation of red blood cell ghosts in a simple shear flow, Phys. Fluids 10 (1998) 1834–1845.
[49] P. Bagchi, Mesoscale simulation of blood flow in small vessels, Biophys. J. 92 (2007) 1858–1877.

[50] T. Ye, H. Li, K.Y. Lam, Modeling and simulation of microfluid effects on deformation behavior of a red blood cell in a capillary, Microvasc. Res. 80 (2010) 453–463.
[51] A. Jafari, P. Zamankhan, S.M. Mousavi, P. Kolari, Numerical investigation of blood flow. Part II: in capillaries, Commun. Nonlinear Sci. Numer. Simul. 14 (2009) 1396–1402.
[52] N. Minc, D. Burgess, F. Chang, Influence of cell geometry on division-plane positioning, Cell 144 (2011) 414–426.
[53] D.J. Eyre, Computational and Mathematical Models of Microstructural Evolution, The Material Research Society, Warrendale, PA, 1998.
[54] D.J. Eyre, An unconditionally stable one-step scheme for gradient systems, 1998. Unpublished article: www.math.utah.edu/~eyre/research/methods/stable.ps.
[55] J. Kim, H.-O. Bae, An unconditionally stable adaptive mesh refinement for Cahn–Hilliard equation, J. Korean Phys. Soc. 53 (2008) 672–679.
[56] J. Kim, Phase-field models for multi-component fluid flows, Commun. Comput. Phys. 12 (3) (2012) 613–661.
[57] H.G. Lee, J. Kim, Accurate contact angle boundary conditions for the Cahn–Hilliard equations, Comput. Fluids 44 (2011) 178–186.
[58] Y. Li, H.G. Lee, J. Kim, A fast, robust, and accurate operator splitting method for phase-field simulations of crystal growth, J. Cryst. Growth 321 (2011) 176–182.
[59] A. Karma, W.-J. Rappel, Quantitative phase-field modeling of dendritic growth in two and three dimensions, Phys. Rev. E 57 (1998) 4323–4349.
[60] J. Rosam, P. Jimack, A. Mullis, A fully implicit, fully adaptive time and space discretization method for phase-field simulation of binary alloy solidification, J. Comput. Phys. 225 (2007) 1271–1287.
[61] Y. Li, J. Kim, A fast and accurate numerical method for medical image segmentation, J. Korean Soc. Ind. Appl. Math. 14 (2010) 201–210.